CFD simulation of flow behind overflooded obstacle

Yvetta Velísková[1*], Zdeněk Chára[2], Radoslav Schügerl[1], Renáta Dulovičová[1]

[1] Institute of Hydrology of the Slovak Academy of Sciences, Dúbravská cesta 9, 841 04 Bratislava, Slovakia.
[2] Institute of Hydrodynamics of the Czech Academy of Sciences, v. v. i., Pod Patankou 30/5, 166 12 Prague 6, Czech Republic.
[*] Corresponding author. E-mail: veliskova@uh.savba.sk

Abstract: This paper deals with studying of two topics – measuring of velocity profile deformation behind a over-flooded construction and modelling of this velocity profile deformation by computational fluid dynamics (CFD). Numerical simulations with an unsteady RANS models - Standard k-ε, Realizable k-ε, Standard k-ω and Reynolds stress models (ANSYS Fluent v.18) and experimental measurements in a laboratory flume (using ADV) were performed. Results of both approaches showed and affirmed presence of velocity profile deformation behind the obstacle, but some discrepancies between the measured and simulated values were also observed. With increasing distance from the obstacle, the differences between the simulation and the measured data increase and the results of the numerical models are no longer usable.

Keywords: Velocity profile; Computational fluid dynamics (CFD); Free surface flow; Bridge; ADV; Laboratory flume; Numerical simulation; RANS models.

INTRODUCTION

Researchers typically address problems in science and engineering through two complementary approaches: experimental and analytical (or numerical). In many applications the governing equations are nonlinear and analytical solutions are very often not available. In addition, fluid mechanics applications are often multidimensional in nature and time-dependent. Accurate modelling of velocity profile is essential for estimating discharge capacity, flow conditions in a stream or the impact of various constructions to morphological stability of stream bed, etc. The measurement of instantaneous velocities in water flows has long been a challenging issue. Observing a velocity distribution inside flowing water streams is not easy in natural conditions. Existing flow velocity will not be uniform in the stream neither without nor with obstacles.

In practice of civil engineering numerical models are accepted as a means of predicting water flow (Kerenyi et al., 2008; Versteegh, 1990). While for the final design of some important projects or hydraulic problems the physical model scale are being built (Evangelista et al., 2017; Kocaman and Ozmen-Cagatay, 2012), the preliminary designs are more and more tested by numerical models (Kerenyi et al., 2008; Nagata et al., 2005; Schmidt and Thiele, 2002). But each numerical model should be verified, so the objective of this work was to verify the numerical simulation by measurement in laboratory condition.

Flows may be considerably affected by the presence of natural or artificial obstacles. In the case of severe floods, for example due to dam- or dike-break, the influence of such obstacles is even amplified. Neglecting this influence in numerical simulations of such flows could lead to heavy misinterpretation. The presence of obstacles is common in river as well in minor bed (bridge piers) as in floodplains (abutments, dikes, trees and vegetation, debris from former floods, etc.). Moreover, if the river embankments are overtopped or the flood dikes breached, flow will occur in areas that are normally not subject to inundation, not prepared to support such a hazard, and thus presenting a series of obstacles, for example roads, railways, dwellings, industrial and commercial structures, etc. (Frazao et al., 2004; Laks et al., 2017).

The impact of obstacles in the riverbed on changing the velocity profile can be studied through a variety of experimental and numerical approaches. In this paper, we focused on a simple model of a bridge structure located in a rectangular laboratory flume and to determine the effect of this model on the velocity field behind the obstacle.

Identification of computational fluid dynamics (CFD) is one of the aspects that must be taken into account when we make or pick out the numerical model for application. Numerical modelling of the flow structures surrounding these obstructions is challenging, yet it represents an important tool for velocity profile assessment. Several three-dimensional CFD models have been already applied to typical hydraulic engineering cases, as through bridge piers and dam breaks. For instance, Shen and Diplas (2008) conducted numerical simulations using CFD models to assess their ability to produce complex flow patterns triggered by the presence of obstacles at various discharges. It is concluded that numerical models can provide an accurate description of the heterogeneous velocity patterns favored by many aquatic species over a broad range of flows, especially under deep flow conditions when the various obstructions are submerged. A comprehensive study of the CFD was provided by Olsen (1999). Numerical modelling of flow around a submerged obstacle is described for example by Janssen et al. (2012), Keylock et al. (2012), Baranya et al. (2012), Stoesser et al. (2015), and Zhang et al. (2009).

The finite volume method was used to perform numerical simulations and in the physical model the velocity field was measured using the ADV (Acoustic Doppler Velocimetry) method. ADV method has become the tool of choice for mapping velocity fields that are used to assess aquatic habitat and validate numerical models (Mueller et al., 2007). Takashi et al. (2004) present velocity profiles and accurate flow rate measurements in open channel flow using ultrasonic Doppler method.

DESCRIPTION OF MODEL SITUATION

As a model situation the flow condition in rectangular cross section shape channel was chosen. It is well-known that during a flood on a creek or a small river, a bridge opening may run completely full or even the entire bridge may be submerged by

the flow (Kerenyi et al., 2008; Picek et al., 2007). Additionally, presence of aquatic vegetation is typical and frequent in lowland channels (Fig. 1). So, the shape of the used obstacle expresses the reduction of cross-section profile flow area as a result of dense vegetation and a bridge construction during a flood event. It is very difficult to obtain any information of flow characteristics on bridge constructions during flood events. Therefore a physical modelling or CFD simulations are used to obtain reasonable data. In this paper we focused on the use of CFD simulations with verification on a physical model.

Fig. 1. Lowland channel part with vegetation and a bridge construction (Chotárny channel, Žitný Ostrov).

NUMERICAL SIMULATIONS

As it was mentioned above, the objective of this study was to perform a comparison of the CFD simulations with an experimental observation. We tested four turbulence models - Standard k-ε, Realizable k-ε, Standard k-ω and Reynolds stress models which all are implemented in the CFD software ANSYS-Fluent 18.0.

The k-ε models have become one of the most widely used turbulence models as it provides robustness, economy and reasonable accuracy for a wide range of turbulent flows. The Standard k-ε model calculates the turbulent viscosity from the equation

$$\mu_t = \rho C_\mu \frac{k^2}{\varepsilon} \tag{1}$$

where k is the turbulent kinetic energy, ε is the rate of dissipation of the turbulent kinetic energy and C_μ is a constant. To obtain the turbulent kinetic energy and its rate of dissipation additional two equations have to be solved. For the incompressible flow condition the equations can be written as

$$\frac{\partial}{\partial t}(\rho k) + \frac{\partial}{\partial x_i}(\rho k u_i) = \frac{\partial}{\partial x_j}\left[\left(\mu + \frac{\mu_t}{\sigma_k}\right)\frac{\partial k}{\partial x_j}\right] + \mu_t S^2 - \rho\varepsilon \tag{2a}$$

$$\frac{\partial}{\partial t}(\rho\varepsilon) + \frac{\partial}{\partial x_i}(\rho\varepsilon u_i) = \frac{\partial}{\partial x_j}\left[\left(\mu + \frac{\mu_t}{\sigma_\varepsilon}\right)\frac{\partial\varepsilon}{\partial x_j}\right] +$$
$$C_{1\varepsilon}\frac{\varepsilon}{k}\mu_t S^2 - C_{2\varepsilon}\rho\frac{\varepsilon^2}{k} \tag{2b}$$

The Prandtl numbers σ_k and σ_ε have values of 1.0 and 1.3, respectively. The model constants C_μ, $C_{1\varepsilon}$ and $C_{2\varepsilon}$ of 0.09, 1.44 and 1.92 were used.

The Realizable k-ε model features two main differences from the Standard k-ε model. It uses a new equation for the turbulent viscosity and the dissipation rate transport equation has been derived from the equation for the transport of the mean-square vorticity fluctuation. The equation for the turbulent kinetic energy is the same as for the Standard k-ε model. Although the equation for the turbulent viscosity is formally identical with the equation (1) the term C_μ is no more constant

$$C_\mu = \frac{1}{A_0 + A_s \frac{k}{\varepsilon}\sqrt{S_{ij}S_{ij} + \tilde{\Omega}_{ij}\tilde{\Omega}_{ij}}} \tag{3}$$

$$\tilde{\Omega}_{ij} = \overline{\Omega}_{ij} - \varepsilon_{ijk}\omega_k - 2\varepsilon_{ijk}\omega_k, \quad \overline{\Omega}_{ij} = \frac{1}{2}\overline{\left(\frac{\partial u_i}{\partial x_j} - \frac{\partial u_j}{\partial x_i}\right)},$$
$$S_{ij} = \frac{1}{2}\left(\frac{\partial u_i}{\partial x_j} + \frac{\partial u_j}{\partial x_i}\right) \tag{4}$$

$$A_0 = 4.04, \quad A_s = \sqrt{6}\cos\left[\frac{1}{3}\cos^{-1}\left(\sqrt{6}\frac{S_{ij}S_{jk}S_{ki}}{\sqrt{S_{ij}S_{ij}}}\right)\right] \tag{5}$$

$$\frac{\partial}{\partial t}(\rho\varepsilon) + \frac{\partial}{\partial x_i}(\rho\varepsilon u_i) = \frac{\partial}{\partial x_j}\left[\left(\mu + \frac{\mu_t}{\sigma_\varepsilon}\right)\frac{\partial\varepsilon}{\partial x_j}\right] +$$
$$\rho C_1 S\varepsilon - \rho C_2 \frac{\varepsilon^2}{k + \sqrt{\frac{\mu\varepsilon}{\rho}}} \tag{6}$$

$$C_1 = \max\left[0.43, \frac{\eta}{\mu + 5}\right], \quad \eta = S\frac{k}{\varepsilon}, \quad S = \sqrt{2S_{ij}S_{ij}}$$

The model constants are $\sigma_k = 1.0$, $\sigma_\varepsilon = 1.2$ and $C_2 = 1.9$.

In the Standard k-ω model ω is an inverse time scale that is associated with the turbulence (specific dissipation rate). The turbulent viscosity is calculated for the equation

$$\mu_t = \alpha^* \frac{\rho k}{\omega} \tag{7}$$

where the parameter α^* is a damping coefficient. For the high-Reynolds form of this model the damping coefficient equals 1. The equations for the k and ω are

$$\frac{\partial}{\partial t}(\rho k) + \frac{\partial}{\partial x_i}(\rho k u_i) = \frac{\partial}{\partial x_j}\left[\left(\mu + \frac{\mu_t}{\sigma_k}\right)\frac{\partial k}{\partial x_j}\right] +$$
$$\mu_t S^2 - \rho\beta^* f_\beta k\omega \tag{8a}$$

$$\frac{\partial}{\partial t}(\rho\omega) + \frac{\partial}{\partial x_i}(\rho\omega u_i) = \frac{\partial}{\partial x_j}\left[\left(\mu + \frac{\mu_t}{\sigma_\omega}\right)\frac{\partial\omega}{\partial x_j}\right] +$$
$$\alpha\frac{\omega}{k}\mu_t S^2 - \rho\beta_i f_\beta \omega^2 \tag{8b}$$

where

$$f_{\beta^*} = \begin{cases} 1 & X_k \le 0 \\ \dfrac{1+680\,X_k^2}{1+400\,X_k^2} & X_k > 0 \end{cases} \quad X_k = \dfrac{1}{\omega^3}\dfrac{\partial k}{\partial x_j}\dfrac{\partial \omega}{\partial x_j} \tag{9}$$

$$\beta^* = \beta_\infty^* \left[\dfrac{0.267 + (0.125\,\mathrm{Re}_t)^4}{1+(0.125\,\mathrm{Re}_t)^4} \right], \quad \mathrm{Re}_t = \dfrac{\rho k}{\mu \omega} \tag{10}$$

$$f_\omega = \dfrac{1+70X_\omega}{1+80X_\omega}, \quad X_\omega = \left| \dfrac{\Omega_{ij}\Omega_{jk}S_{ki}}{\left(\beta_\infty^* \omega\right)^3} \right| \tag{11}$$

$$\alpha^* = \alpha_\infty^* \left(\dfrac{0.024 + 0.167\,\mathrm{Re}_t}{1+0.167\,\mathrm{Re}_t} \right), \quad \alpha = \dfrac{\alpha_\infty}{\alpha^*}\left(\dfrac{0.111+0.339\,\mathrm{Re}_t}{1+0.339\,\mathrm{Re}_t} \right) \tag{12}$$

The model constants are $\alpha_\infty^* = 1.0$, $\alpha_\infty = 0.52$, $\beta_\infty^* = 0.09$, $\beta_i = 0.072$, $\sigma_k = 1.0$, $\sigma_\omega = 1.2$.

The Reynolds stress model closes the Reynolds-Averaged Navier-Stokes equations by solving additional transport equations for the six independent Reynolds stresses

$$\dfrac{\partial}{\partial t}\left(\rho \overline{u_i' u_j'}\right) + \dfrac{\partial}{\partial x_k}\left(\rho u_k \overline{u_i' u_k'}\right) = \dfrac{n!}{r!(n-r)!}$$

$$-\dfrac{\partial}{\partial x_k}\left[\rho \overline{u_i' u_j' u_k'} + \overline{p'\left(\delta_{kj}u_i' + \delta_{ik}u_j'\right)} \right] + \dfrac{\partial}{\partial x_k}\left[\mu \dfrac{\partial}{\partial x_k}\left(\overline{u_i' u_j'}\right) \right] -$$

$$\rho\left(\overline{u_i' u_k'}\dfrac{\partial u_j}{\partial x_k} + \overline{u_j' u_k'}\dfrac{\partial u_i}{\partial x_k} \right) + \overline{p'\left(\dfrac{\partial u_i'}{\partial x_j} + \dfrac{\partial u_j'}{\partial x_i}\right)} -$$

$$2\mu\overline{\dfrac{\partial u_i'}{\partial x_k}\dfrac{\partial u_j'}{\partial x_k}} - 2\rho\Omega_k\left(\overline{u_j' u_m'}\varepsilon_{ikm} + \overline{u_i' u_m'}\varepsilon_{jkm} \right) \tag{13}$$

where $\varepsilon_{i,jkm}$ is Levi-Civita symbol. In our simulations we have used the Reynolds stress model with a linear pressure strain term.

Two-phase VOF (Volume of Fluid) model was used to simulate the free water level. To increase the water level in the channel, a 60 mm height sharp edge weir was placed at the end of the simulated section. The shape of the entrance section with the inclined top wall has been chosen to ensure that the inlet to the channel is fully flooded. A constant velocity profile was assumed at the channel inlet. The water from the channel drained through the bottom opening in an outlet chamber. The schematic view of the computation domain is shown in Fig. 2.

The direction of the flow is from the left to the right. The length of the simulated channel was 3500 mm, followed by a 600 mm calming chamber. The upstream edge of the obstacle was located 1500 mm from the inlet profile. The width of the channel was 400 mm but only half of the channel was modelled and the axis plane was treated as a symmetry boundary condition. The dimensions and the orientation of the bridge obstacle were the same as on the physical model (Fig. 4) except a small part close to a connection of the upstream pillar and the side wall. The boundary layers on the solid surfaces were meshed by a structured mesh and the rest of the computational domain was meshed by tetrahedral cells. Sizes of cells varied from 0.1 to 3.5 mm. All numerical simulations were performed as unsteady simulations using the influence of gravity. The flow discharge was the same as in the case of the physical model – 39 x 10^{-3} m^3 s^{-1}. On the beginning of the simulation the channel was filled by water up to a level 250 mm.

LABORATORY MEASUREMENTS

Measurements were performed in a laboratory flume at the Institute of Hydrodynamics of the Czech Academy of Sciences. Laboratory flume had a rectangular cross section shape, length equals 25 m and width 400 mm (Fig. 3). A downstream weir with horizontal jalousies was used to keep the water level on the height around 250 mm and the discharge was regulated on a value of 39 x 10^{-3} m^3 s^{-1}.
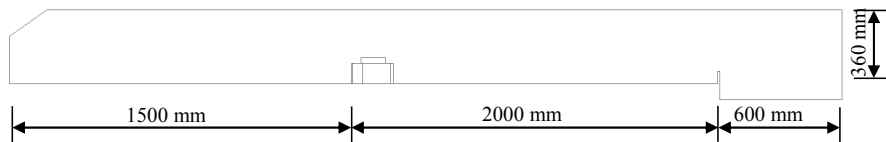

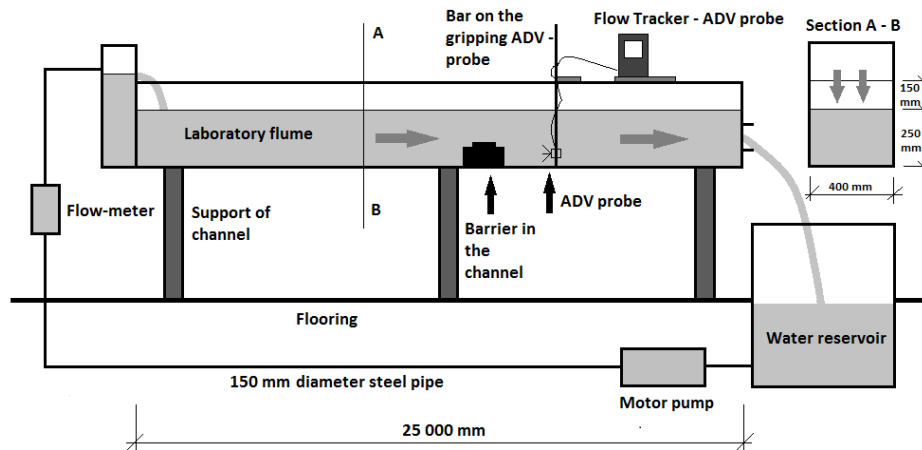**Fig. 2.** Schematic view of the computational domain.

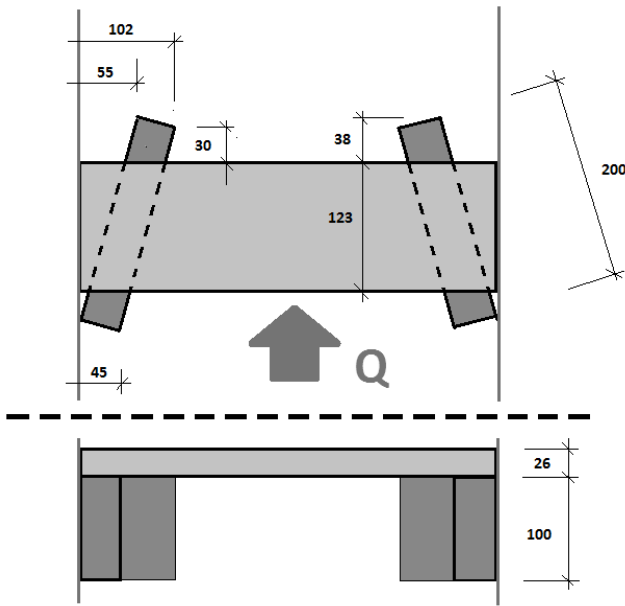**Fig. 3.** Scheme of laboratory flume with the wooden barrier location.

Fig. 4. Ground plan of obstacle and sight on the obstacle in the course of flow in laboratory flume.

As a measuring device there was used the ADV FlowTracker 3D probe. Many "aquatic" scientists employ ADV to characterise flow conditions (Carollo et al., 2002; Kim et al., 2000; Nikora et al., 1998). Compared to the thermal anemometry (hot film, hot wire, hot bead) and other invasive measurement techniques, like e.g. mechanical current-meters or electromagnetic sensors, the ADV has the advantage of being non-invasive, as the measuring volume is located some distance away from the actual probe. Acoustic instruments have relatively large sampling volumes, but they add the possibility of application in field conditions. In general, ADV are more straightforward to use, more robust, and easier to modify for field work than the other techniques. ADV use can limit mainly the accuracy of turbulence intensities, especially when making measurements close to the bed or in flows where large spatial gradients are present (Dombroski and Crimaldi, 2007).

The technique relies on the Doppler shift principle to measure the velocity of suspended scattering particles that are assumed to move passively with the flow. The ADV conducts 3 component current measurements in a sampling volume below the transmit-transducer. Sound bursts of known duration and frequency are emitted by the central transmitter and subsequently reflected back by suspended particles moving through the sampling volume. The reflected signals that are shifted in frequency (Doppler shift) are collected by the three receivers that surround the transmitter. The magnitude of the frequency shift is proportional to the velocity of the reflecting particles (Precht et al., 2006).

During the experiments it was applied so-called "General Mode" of ADV FlowTracker 3D probe (SonTek, 2009). This mode allows to measure velocity components in any measured point grid. In the first step, the measurements were carried out in profile, in which the flow is not disturbed – it means without any barrier. In the second phase, we placed a wooden barrier to the laboratory flume, which changed flow conditions and velocity component fields.

The obstacle was made from three prisms: two prisms on the flume bottom were stored obliquely at the angle 30° to the direction of flow of water in the flume. Bottom prisms have dimensions 50 x 100 x 200 mm. For these prisms (Fig. 4), we laid and attached perpendicularly to the flow direction upper prism with dimensions (26 x 123 x 400) mm. We measured the distribution of the velocity field at four profiles at a distance x_i = 70, 170, 300 and 900 mm from the barrier (Fig. 5) for information how velocity profile deformation damps down.

The measurement grid was created by different verticals along the flume width. All measurements were performed only in one half of cross-section profile because the flume and the obstacle were symmetrical by central axis. We selected the verticals in distance y_i = 70, 100, 130, 160, 190 and 220 mm from right side wall of the flume for profiles behind the obstacle, with the aim to take the velocity distribution in more details. Point velocity components v_x, v_y, v_z were measured at 7 different heights in each vertical. Heights of measured points in the verticals were z_i = 40, 80, 100, 120, 140, 160 and 180 mm from the bottom of the laboratory flume. The grid of measuring points in cross-section profiles was identical for all measurements and tests. The origin of the co-ordinate system is at the
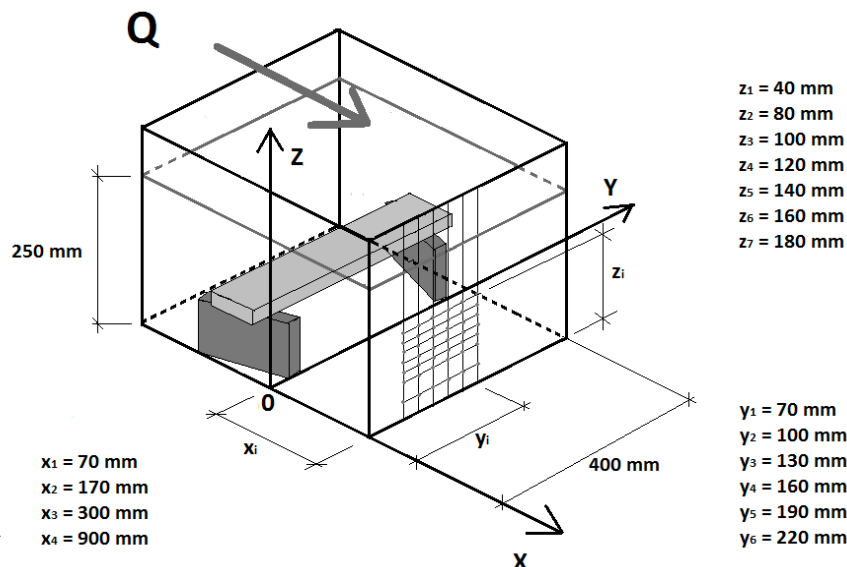

Fig. 5. Scheme of wooden obstacle in laboratory flume and location of measuring points of velocity components.
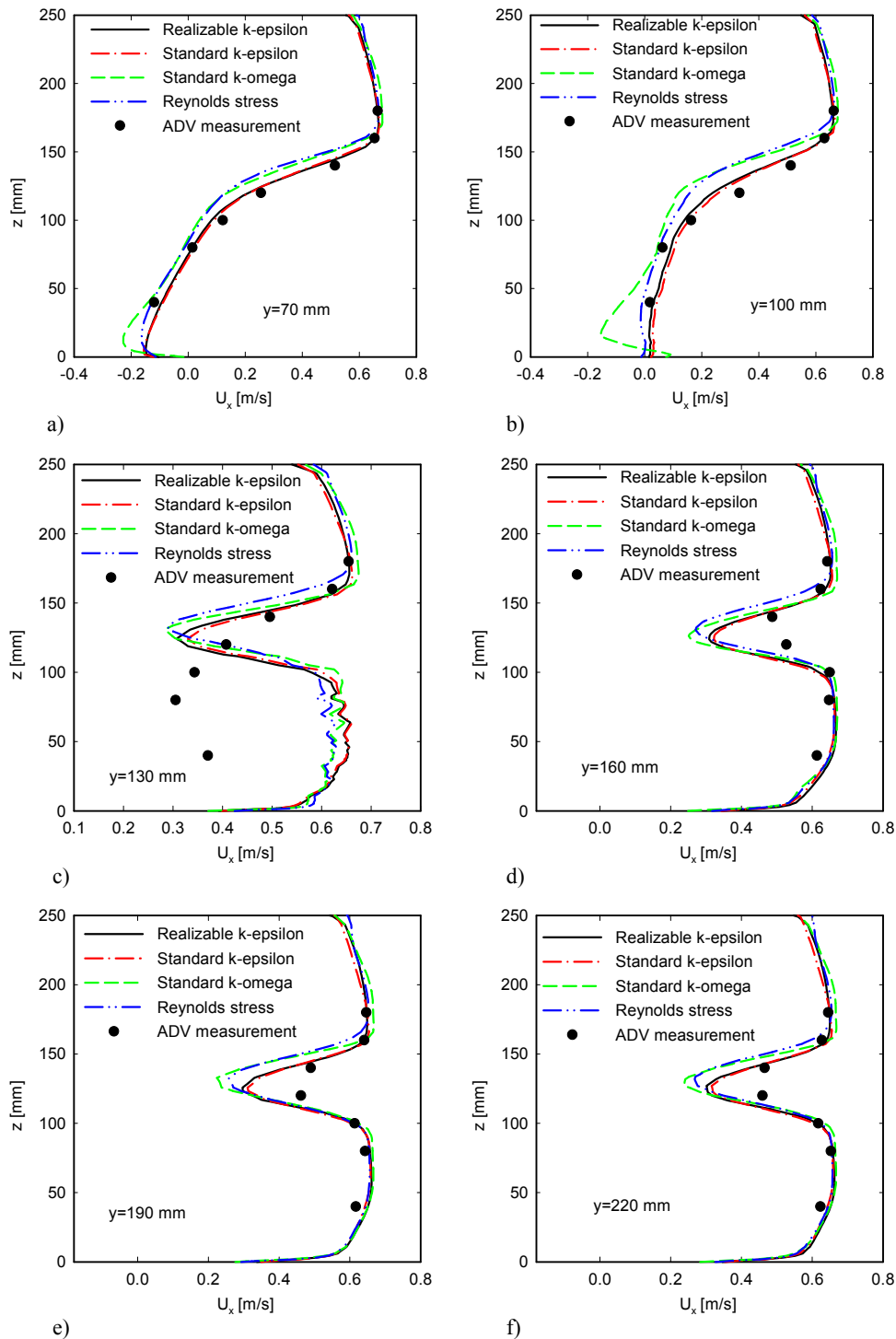
Fig. 6. Velocity profiles at the distance 70 mm behind the obstacle – a) y = 70 mm from the side wall, b) y = 100 mm, c) y = 130 mm, d) y = 160 mm, e) y = 190 mm, f) y = 220 mm.

bottom of the side wall of the channel. The longitudinal co-ordinate (*x*) starts at the position corresponding to the downstream edge of the obstacle.

Measurement time (*t*) was 240 seconds in each of the measuring grid point in the profile without barrier impact. Measurements results showed satisfactory stability of the probe. Because flow conditions behind the barrier are more complicated, the time of measurement for point velocity components in the profiles behind the barrier was increased to 300 seconds in each measured grid point.

RESULTS

The measured longitudinal velocity components were compared with the numerical simulations and the results are shown in Figs. 6–9.

Fig. 6 shows the measured and simulated velocity profiles at a distance of 70 mm behind the obstacle. In this figure we can see quite good agreement between the measured and simulated values of the longitudinal component of the velocity. The only exception is the velocity profile at *y* = 130 mm from the side-
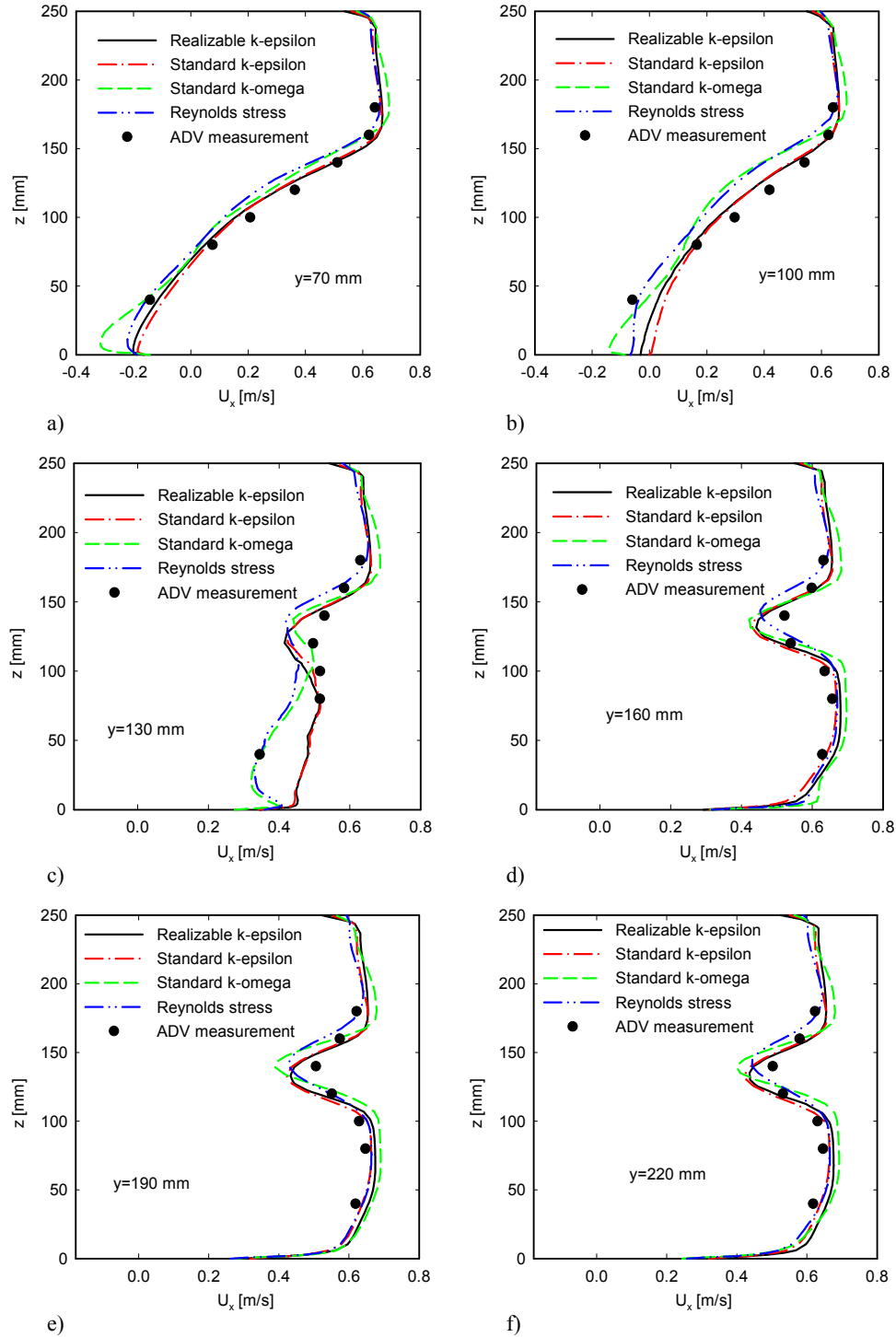
Fig. 7. Velocity profiles at the distance 170 mm behind the obstacle – a) y = 70 mm from the side wall, b) y = 100 mm, c) y = 130 mm, d) y = 160 mm, e) y = 190 mm, f) y = 220 mm.

wall where the simulated values already show the effect of the lower opening of the obstacle. This discrepancy can be caused on the one hand by the size of the ADV probe area being relatively large (in the order of tens of mm³) and, on the other hand, by the large velocity component gradients in this area and also by velocity component fluctuations in measured volume during the measured period (Precht et al., 2006; Voulgaris and Trowbridge, 1998). Similar results were obtained for the velocity profiles measured at x = 170 mm. The results are shown in Fig. 7. Here, a relatively good match between the measured and

simulated values of the longitudinal velocity component was also observed. However, with increasing distance from the obstacle, there are visible differences between measured and simulated data. Fig. 8 shows the velocity profiles measured at a distance of x = 300 mm. Differences between measured and simulated velocities can be observed mainly in the bottom part, close to the sidewall, where the measured velocities are significantly higher than the velocity determined from the simulation. In the case of the vertical at y = 160 mm from the sidewall the simulated velocities are higher. These differences are even
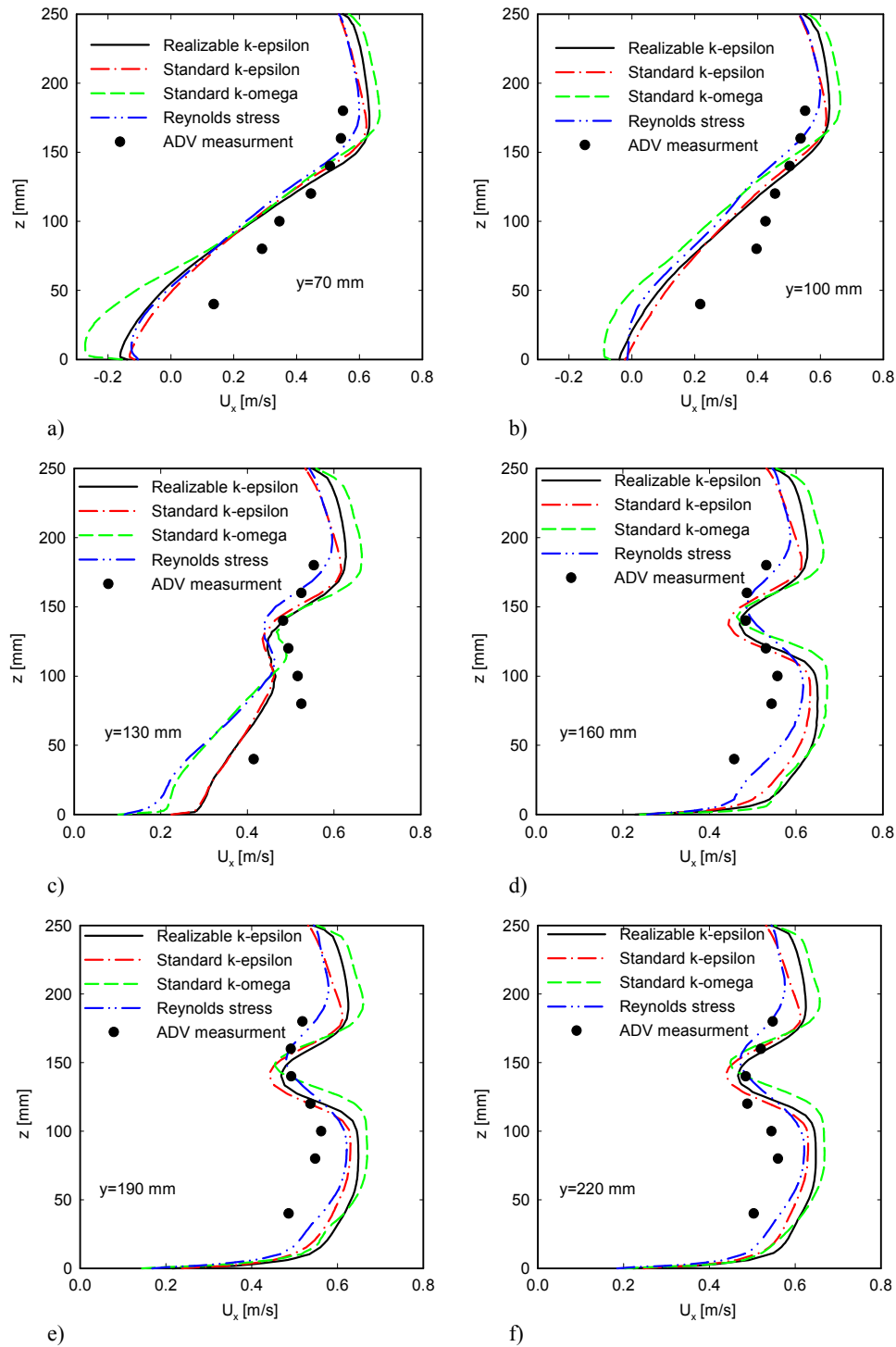
Fig. 8. Velocity profiles at the distance 300 mm behind the obstacle – a) *y* = 70 mm from the side wall, b) *y* = 100 mm, c) *y* = 130 mm, d) *y* = 160 mm, e) *y* = 190 mm, f) *y* = 220 mm.

more pronounced for the velocity profiles measured at the distance $x = 900$ mm, which are shown in Fig. 9. While the longitudinal velocities in the physical model are higher close to the side wall, towards the centre of the flume the measured velocities decrease. On the contrary the simulation still shows the influence of the bottom opening of the obstacle and therefore the highest velocities are observed in the centre part of the channel close to the bottom. Fig. 9 also shows the results of the measurement of the velocity profiles in case when the flume flow is unobstructed. It turns out that due to the obstacle there

is a significant decrease in the velocity at the bottom part of the flume and even in this distance from the obstacle edge the impact of it does not disappear.

CONCLUSIONS

The paper presents the results of numerical simulations of velocity profile deformation behind the over flooded obstacle in the rectangular laboratory flume using the RANS models - Standard *k-ε*, Realizable *k-ε*, Standard *k-ω* and Reynolds stress
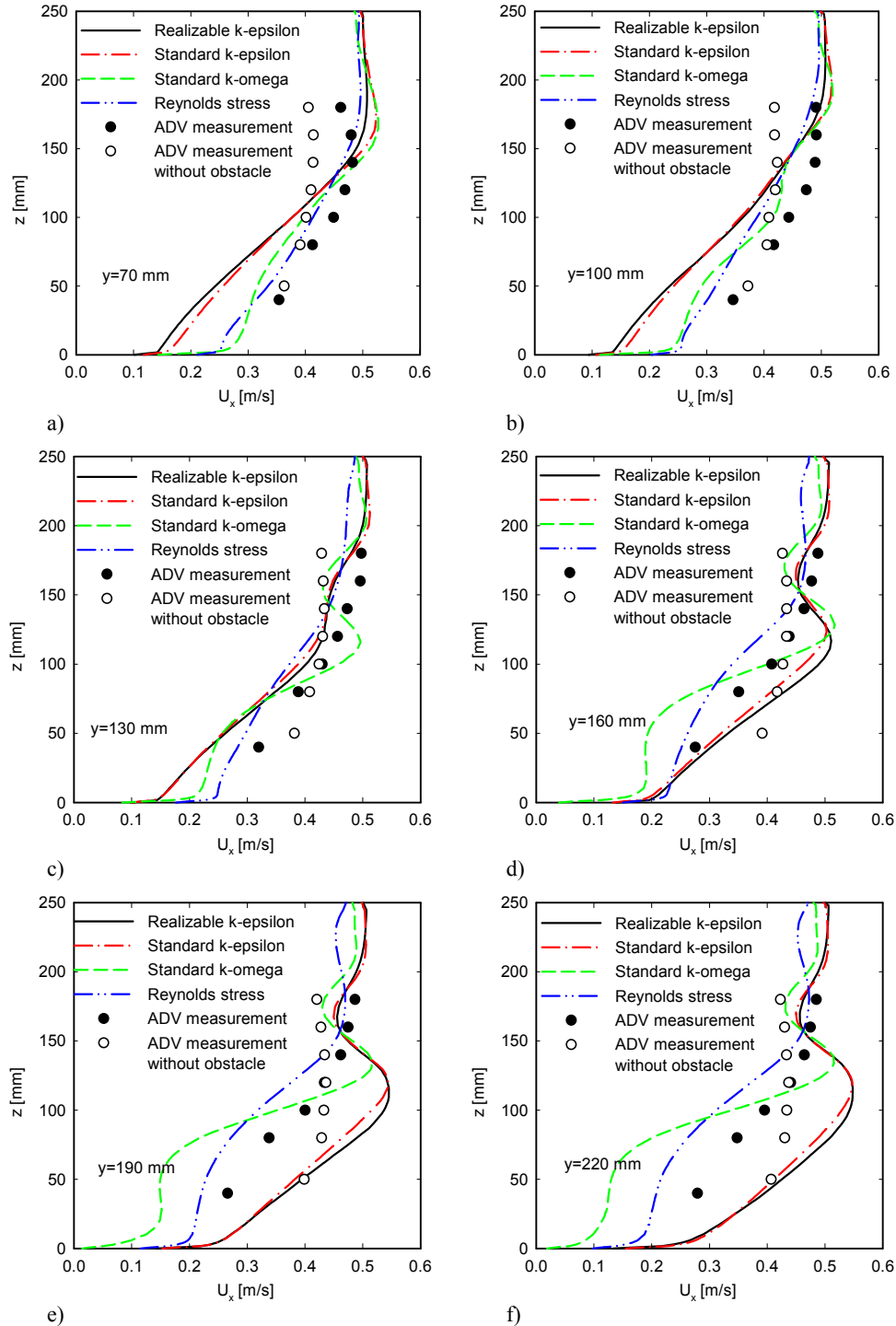
Fig. 9. Velocity profiles at the distance 900 mm behind the obstacle – a) $y = 70$ mm from the side wall, b) $y = 100$ mm, c) $y = 130$ mm, d) $y = 160$ mm, e) $y = 190$ mm, f) $y = 220$ mm.

models. In addition, the measurements by ADV device were performed on the physical model for verification of simulation results. Dimensions of simulated geometry matched dimensions on the physical model. It has been confirmed that simulation outputs of all models give usable results only in the area up to about 0.2 m behind the obstacle, which is approximately equivalent to double of the obstacle height and approximately equal to water depth. With the increasing distance from the obstacle, the differences between the simulation and the measured data increase and the chosen numerical approach no longer produces usable results.

REFERENCES

Baranya, S., Olsen, N.R.B., Stoesser, T., Sturm, T., 2012. Three-dimensional rans modeling of flow around circular piers using nested grids. Engineering Applications of Computational Fluid Mechanics, 6, 4, 648–662. http://doi.org/10.1080/19942060.2012.11015449

Carollo, F.G., Ferro, V., Termini, D., 2002. Flow velocity measurements in vegetated channels. J. Hydraul. Eng.-ASCE, 128, 7, 664–673. ISSN 0733-9429.

Dombroski, D.E., Crimaldi, J., 2007. The accuracy of acoustic Doppler velocimetry measurements in turbulent boundary layer flows over a smooth bed. Limnology and Oceanography: Methods, 5, 23–33. ISSN 1541-5856.

Evangelista, S., Giovinco, G., Kocaman, S., 2017. A multi-parameter calibration method for the numerical simulation of morphodynamic problems. J. Hydrol. Hydromech., 65, 175–182. DOI: 10.1515/johh-2017-0014.

Frazao, S.S., Noel, B., Zech, Y., 2004. Experiments of dam-break flow in the presence of obstacle. http://www.impact-project.net/AnnexII_DetailedTechnicalReports/AnnexII_PartB_WP3/RF_Soares_et_al_Obstacle_B1-226.pdf

Janssen, F., Cardenas, M.B., Sawyer, A.H., Dammrich, T., Krietsch J., de Beer, D., 2012. A comparative experimental and multiphysics computational fluid dynamics study of coupled surface-subsurface flow in bed forms. Water Resources Research, 48, 8, 1–16. ISSN 1944-7973.

Keylock, C.J., Constantinescu, G., Hardy, R.J., 2012. The application of computational fluid dynamics to natural river channels: Eddy resolving versus mean flow approaches. Geomorphology, 179, 1–20. http://doi.org/10.1016/j.geomorph.2012.09.006

Kerenyi, K., Sofu, T., Guo, J., 2008. Using supercomputers to determine bridge loads. Public Roads, 72, 2, Publication Number: FHWA-HRT-08-006. https://www.fhwa.dot.gov/publications/publicroads/08sep/05.cfm

Kim, S.C., Friedrichs, C.T., Maa, J.P.Y., Wright, L.D., 2000. Estimating bottom stress in tidal boundary layer from acoustic Doppler velocimeter data. J. Hydraul. Eng.-ASCE, 126, 6, 399–406. ISSN 0733-9429.

Kocaman, S., Ozmen-Cagatay, H., 2012. The effect of lateral channel contraction on dam break flows: Laboratory experiment. Journal of Hydrology, 432–433, 145–153. DOI: 10.1016/j.jhydrol.2012.02.035.

Laks, I., Szoszkiewicz K., Kałuża, T., 2017. Analysis of in situ water velocity distributions in the lowland river floodplain covered by grassland and reed marsh habitats - a case study of the bypass channel of Warta River (Western Poland). J. Hydrol. Hydromech., 65, 325–332. DOI: 10.1515/johh-2017-0021.

Mueller, D.S., Abad, J.D., García, C.M., Gartner, J.W., García, M.H., Oberg, K.A., 2007. Errors in acoustic profiler velocity measurements caused by flow disturbance. Journal of Hydraulic Engineering, 133, 12, 1411–1420. DOI: 10.1061/ASCE0733-94292007133:121411 C.

Nagata, N., Hosoda, T., Nakato, T., Muramoto, Y., 2005. Three-Dimensional Numerical Model for Flow and Bed Deformation around River Hydraulic Structures. Journal of Hydraulic Engineering, 131, 12, 14. ISSN 0733-9429.

Nikora, V.I., Suren, A.M., Brown, S.L.R., Biggs, B.J.F., 1998. The effects of the moss *Fissidens rigidulus* (*Fissidentaceae*: *Musci*) on near-bed flow structure in an experimental cobble bed flume. Limnol. Oceanogr, 43, 6, 1321–1331.

Olsen, N.R.B., 1999. Computational Fluid Dynamics in Hydraulic and Sedimentation Engineering. The Norwegian University of Science and Technology, 65 p. ISBN 82-7598-041-0.

Picek, T., Havlik, A., Mattas D., Mares, K., 2007. Hydraulic calculation of bridges at high water stages. Journal of Hydraulic Research, 45, 3, 400–406. doi.org/10.1080/00221686.2007.9521773

Precht, E., Janssen, F., Huettel, M., 2006. Near-bottom performance of the Acoustic Doppler Velocimeter (ADV) – a comparative study. Aquatic Ecology, 40, 481–492. DOI: 10.1007/s10452-004-8059-y.

Schmidt, S., Thiele, F., 2002. Comparison of numerical methods applied to the flow over wall-mounted cubes. Int. J. Heat Fluid Flow, 23, 3, 330–339. ISSN 0142-727X.

Shen, Y., Diplas, P., 2008. Application of two- and three-dimensional computational fluid dynamics models to complex ecological stream flows. Journal of Hydrology, 348, 1–2, 195–214. ISSN 0022-1694.

SonTek, 2009. FlowTracker Handheld ADV Technical Manual, Firmware Version 3.7, Software Version 2.30 – SonTek/YSI, San Diego, 2009, 126 p.

Stoesser, T., Kara, S., Sturm,W.T., Mulahasan, S., 2015. Flow dynamics through a submerged bridge opening with over-topping. Journal of Hydraulic Research, 53, 2, 186–195. ISSN 0022-1686.

Takashi, A., Sanehiro, W., Hiroshige, K., Masanori, A., Michitsugu, M., 2004. Development of flowrate measurement on open channel flow using ultrasonic Doppler method. In: Proc. 4th International Symposium on Ultrasonic Doppler Method for Fluid Mechanics and Fluid Engineering. Sapporo, pp. 33–36.

Versteegh, J., 1990. The numerical simulation of three-dimensional flow through or around hydraulic structures. PhD Thesis. TU Delft.

Voulgaris, G., Trowbridge, J.H., 1998. Evaluation of the acoustic Doppler velocimeter for turbulence measurements. Journal of Atmospheric and Oceanic Technology, 15, 272–289.

Zhang, H., Nakagawa, H., Kawaike, K., Baba, Y., 2009. Experiment and simulation of turbulent flow in local scour around a spur dyke. International Journal of Sediment Research, 24, 1, 33–45, ISSN 1001-6279.

NOMENCLATURE

μ_t	turbulent viscosity	(kg m^{-1} s^{-1})
ρ	density	(kg m^{-3})
k	turbulent kinetic energy	(m^2 s^{-2})
ε	dissipation rate of turbulent kinetic energy	(m^2 s^{-3})
u_i	i-velocity component	(m s^{-1})
u_i'	i-velocity component fluctuation	(m s^{-1})
x_i	i-coordinate	(m)
S_{ij}	strain rate tensor	(s^{-1})
Ω_{ij}	rate-of-rotation tensor	(s^{-1})
S	modulus of the strain tensor	(s^{-1})
ω	specific dissipation rate (ε/k)	(s^{-1})
ω_k, Ω_k	angular velocity	(s^{-1})

Note: Colour version of Figures can be found in the web version of this article.